

Unique Yttria Nanoparticle Strengthening in an Inconel 718 Superalloy Fabricated by Additive Manufacturing

Shengbin Dai, Jiangqi Zhu, Xingchen Yan, Shun Wu, Yang Liu, Xiang Gao, Hamish Fraser, Peter Hodgson, Yuman Zhu,* Martin Heilmaier,* and Aijun Huang*

Oxide dispersion strengthened (ODS) nickel (Ni)-based superalloys are advanced materials known for their outstanding tensile and creep performance at temperatures exceeding 1000 °C. Nevertheless, their conventional synthesis presents a longstanding challenge in cost-effectively producing intricate components for critical applications. In this work, electrostatic self-assembly (ESA) of powders with the laser powder bed fusion (LPBF) process have been successfully combined to produce yttria ODS Inconel 718 (IN718) alloy for the first time. The approach has demonstrated a significant contribution of yttria to the strength of IN718 after the solid solution heat treatment, as evidenced by $\approx 50\%$ improvement in room temperature yield strength with a 0.5 wt.% yttria addition. The addition of yttria by this process leads to a heterogeneous microstructure. This heterogeneous microstructure comprises two distinct grain areas with varying amounts of yttria nanoparticles and dislocation storage. It has been shown that the yield strength increase can be predicted by the combination of both Y_2O_3 dispersion strengthening and dislocation strengthening mechanisms. These findings offer an effective approach to tailor heterogeneous microstructures, unlocking new opportunities for cost-effectively producing high-performance ODS Ni-based superalloy products with excellent mechanical properties.


1. Introduction

Oxide dispersion strengthened (ODS) nickel (Ni)-based superalloys, represented by MA754 and MA6000 (trade-name of Inco Alloys International), are a class of advanced materials comprising a Ni-based matrix that is reinforced with finely dispersed nano-scale oxide particles, such as Y_2O_3 , $YAlO_3$ and $Y_2Ti_2O_7$.^[1–5] Unlike the γ'/γ'' strengthening precipitates formed in many Ni superalloys such as Inconel 625, Inconel 718 (IN718) and Inconel 738, which tend to dissolve as they approach their solvus temperatures, these oxide particles have a markedly higher melting point than the matrix in which they are embedded. This unique feature enables them to effectively impede dislocation glide even at temperatures close to the melting point of Ni-based superalloys, particularly when they are homogeneously distributed in the consolidated products with a diameter smaller than 50 nm (or more precisely

S. Dai, S. Wu, X. Gao, Y. Zhu, A. Huang
Monash Centre for Additive Manufacturing
15–17 Normanby Rd, Notting Hill VIC 3168, Australia
E-mail: yuman.zhu@monash.edu; aijun.huang@monash.edu

S. Dai, S. Wu, X. Gao, Y. Zhu, A. Huang
Department of Materials Science and Engineering
Monash University
Clayton VIC 3800, Australia

S. Dai, J. Zhu, X. Yan
Guangdong Academy of Sciences
Guangdong Institute of New Materials
National Engineering Laboratory for Modern Materials Surface
Engineering Technology
The Key Lab of Guangdong for Modern Surface Engineering Technology
Guangzhou 510650, P. R. China

 The ORCID identification number(s) for the author(s) of this article can be found under <https://doi.org/10.1002/admt.202301421>

© 2023 The Authors. Advanced Materials Technologies published by Wiley-VCH GmbH. This is an open access article under the terms of the Creative Commons Attribution-NonCommercial License, which permits use, distribution and reproduction in any medium, provided the original work is properly cited and is not used for commercial purposes.

DOI: 10.1002/admt.202301421

Y. Liu
Monash Centre for
Electron Microscopy
10 Innovation Walk, Clayton VIC 3800, Australia

H. Fraser
Center for the Accelerated Maturation of Materials
Department of Materials Science and Engineering
The Ohio State University
Columbus, OH 43210, USA

P. Hodgson
Institute for Frontier Materials
Deakin University
Geelong VIC 3217, Australia

M. Heilmaier
Institute for Applied Materials
Karlsruhe Institute of Technology
Engelbert-Arnold-Straße 4, 76131 Karlsruhe, Germany
E-mail: martin.heilmaier@kit.edu

with an interparticle spacing less than 500 nm).^[5–7] As a result, ODS Ni-based superalloys can achieve remarkable performance in terms of tensile and creep (rupture) strength in high-temperature environments, even beyond 1000 °C. These outstanding characteristics make them highly suitable for demanding applications in aerospace, power generation, and nuclear industries, such as turbine blades, combustion chambers, and nuclear reactor components.

Due to the significant difference in density between Ni-based superalloys and oxide particles, the powder metallurgy method has been typically employed to address the issue of agglomeration of oxide particles in Ni-based superalloys associated with conventional casting techniques. One of the most used methods for powder preparation is mechanical alloying (MA).^[7,8] This process involves high-energy input ball milling, which includes cold welding, fracturing and re-welding to ensure the oxide particles are effectively “coated” on the surface of Ni-based superalloy powders.^[8] While this method allows the intimate mixing of oxide particles with the metal powders, it does come with an unavoidable challenge of contamination with gaseous impurities, such as oxygen and nitrogen during the powder mixing process. Additionally, after mechanical alloying, the mixed powders undergo consolidation using techniques such as hot isostatic pressing,^[9] hot extrusion,^[10–11] and spark plasma sintering^[12,13] to achieve the semi-finished product in the form of rods, sheets or foils. However, a significant challenge arises when creating the final products, as expensive machining becomes necessary. This issue becomes more pronounced when dealing with intricate shapes, adding to the overall production costs. Consequently, there is an ongoing and persistent need to explore alternative fabrication methods to overcome these limitations in the long term.

In the past decade, additive manufacturing (AM) has gradually become an enabling technology that has transformed component creation.^[14–17] Unlike traditional subtractive methods as described in the previous paragraph, AM builds components layer by layer, enabling highly efficient production of complex geometries and facilitating rapid prototyping and on-demand manufacturing. To this end, AM is showing its potential to revolutionize the production of ODS superalloys, e.g., Al₂O₃ and HfO₂ doped Fe-Cr-based superalloys fabricated by laser melt deposition (LMD),^[18,19] CeO₂ modified Ni-Cr-based superalloys fabricated by directed laser deposition (DLD),^[20] Particularly, laser powder bed fusion (LPBF), a widely used AM technique, has recently been employed in trials to produce Y₂O₃ strengthened alloys in Inconel 625,^[21] γ/γ′ Ni-based superalloys^[22–24] and IN718.^[25–28] So far, the reported effects of Y₂O₃ particles on strengthening were variable in these alloys. For example, Li et al.^[21] reported a moderate 11% increase (from 394 MPa to 439 MPa) in the room-temperature yield strength of ODS Inconel 625 due to the addition of 1.0 wt.% Y₂O₃ nanoparticles (with an average diameter of 42 nm). Conversely, in as-built IN718 where Laves phases mixed with Y₂O₃ generate, the room-temperature yield strengths did not show any improvements with a 1.0 wt.% addition of Y₂O₃ (average diameter less than 100 nm).^[25] Instead, there was a significant enhancement in elongation, rising from 22% to 28%.^[26] The diverse outcomes from these studies indicate that there should be a clear characterization of discrete Y₂O₃ particles to reveal the effects of Y₂O₃ particles on the microstructures and mechanical properties of IN718 superalloys produced by AM.

Moreover, the original powders used for AM are still mainly manufactured by MA when productivity and convenience are considered. However, the damage to process stability and the deterioration of the process parameter window of LPBF are due to the severe destroy of the spherical powder by MA. Alternatively, to maintain the sphericity of the original powders and reduce the contamination with gaseous impurities during MA, liquid-based powder manufacturing methods controlled by diffusion deposition (DD) and electrostatic deposition (ED) are applied to obtain nano-particle-doped Fe-Cr based superalloys,^[29] 7075 aluminum alloys,^[16,30] Mo-based alloys^[31] and titanium alloy^[32] powders. However, the study on liquid-based powder manufacturing methods applied in ODS Ni-based superalloys is scarcely reported.^[33]

In this study, the LPBF technique is employed to fabricate a Y₂O₃ containing ODS IN718 alloy. To deagglomerate Y₂O₃ nanoparticles, an ED approach with dispersant added, which is called electrostatic self-assembly (ESA),^[30] is utilized for powder preparation before LPBF. The ESA is a low-energy input powder preparation method that enables the introduction of negatively charged oxide nanoparticles onto the positively charged surface of nickel-based superalloy powder. Through the innovative combination of ESA with LPBF in this work, we aim to quantitatively assess the contribution of Y₂O₃ nanoparticles to the strength of IN718, seeking to identify their precise role in determining microstructures and mechanical properties. The work is also expected to show the potential to produce high-performance ODS IN718 alloys with controlled microstructures through AM.

2. Results and Discussion

Prior to implementing the LPBF printing, the ESA approach was employed to assemble Y₂O₃ nanoparticles with IN718 superalloy powder, as described in more detail in Section 4. Y₂O₃ nanoparticles with a normal diameter of 50 nm were used, and two weight percentages of Y₂O₃ were selected: 0.5 wt.% and 1.0 wt.%. This is mainly based on the Y₂O₃ composition in classical ODS Ni-based superalloys, such as MA 754^[1,2,34] and PM1000.^[3] These compositions are referred to as IN718-0.5Y₂O₃ and IN718-1.0Y₂O₃ in the following. The assembly effects of Y₂O₃ nanoparticles on IN718 powder surfaces were examined using scanning electron microscopy (SEM), see **Figure 1**. Comparing the SEM images of IN718-0.5Y₂O₃ with IN718 powders, as shown in Figure 1a,b, it is evident that the spherical shape of the IN718 powder remained intact after ESA. Furthermore, for the IN718-0.5Y₂O₃, numerous Y₂O₃ nanoparticles are observed to be evenly distributed on the surface of IN718 powders, with negligible agglomeration, as shown in the enlarged image inserted in Figure 1b. However, when the Y₂O₃ content reaches 1.0 wt.%, severe agglomeration of Y₂O₃ particles is observed on the surface of IN718 powder particles, as seen in Figure 1c. Based on these results, IN718-0.5Y₂O₃ demonstrates a suitable powder assembly for the LPBF fabrication process as the possibility of agglomeration of the nano-sized oxide particles cannot be ruled out when an excessive amount is added. Due to the agglomeration, not only will the initial mean interparticle spacing of the oxide particles not decrease further when the volume fraction is constant but, more importantly, the homogeneity of the particle arrangements will be undermined

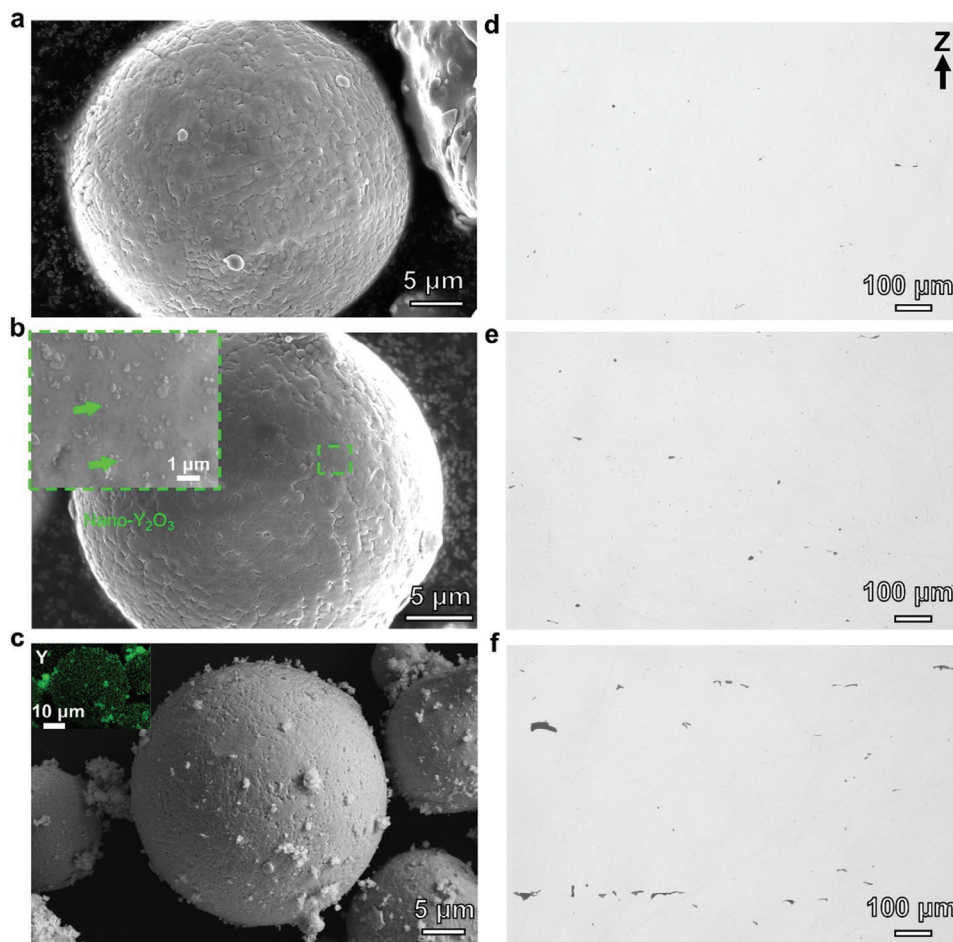


Figure 1. a) SEM image of IN718 virgin powders, b–c) SEM images of IN718 powders decorated by 0.5 wt.% and 1.0 wt.% Y_2O_3 nanoparticles respectively using ESA powder preparation method; d,e,f) Optical microscope images of LPBF samples with 0, 0.5 wt.%, and 1.0 wt.% Y_2O_3 nanoparticle additions, respectively. The “Z” in the image represents the building direction.

resulting in a deterioration in mechanical properties of the ODS Ni-based superalloys.^[34] Nano-sized Y_2O_3 particles (≈ 25 nm) are supposed to have a more significant Zener pinning effect on the grain boundary than micron-sized Y_2O_3 particles (≈ 45 μm).^[35] Therefore, the increase in size of the Y_2O_3 due to the agglomeration is expected to result in coarser grain size at thermodynamic equilibrium, leading to forecasted brittleness of the ODS superalloys with severe agglomeration.

The quality of the powder assembly of IN718-0.5 Y_2O_3 is further supported by evaluating the build quality after LPBF. The optical microscopy (OM) images, as shown in Figure 1d,e, reveal only minor printing defects on the polished surface of the as-printed IN718 and IN718-0.5 Y_2O_3 bulk samples. The measured porosity of the IN718-0.5 Y_2O_3 sample is $\approx 0.17\%$, which is only slightly higher than that of its “pure” (i.e., without dispersoids) IN718 counterpart ($\approx 0.07\%$), see Table 1. In contrast, many relatively large defects were detected in the as-printed IN718-1.0 Y_2O_3 sample (Figure 1f). Consequently, the porosity of the as-built IN718-1.0 Y_2O_3 samples, measuring 0.49%, is approximately seven times higher than that of the IN718 counterpart. The obvious increase in porosity could be related to the severe agglomeration of nanoparticle interaction with the solidification

front^[36,37] (slow down the solidification front velocities) during LPBF where rapid solidification rates (10^4 – 10^7 $K s^{-1}$)^[38] take place. During the solidification, the nanoparticle agglomerations change the surface tension temperature coefficient of melt pool, leaving gaps between the agglomerations and the solidified matrix. Therefore, if a higher fraction of agglomeration of nanoparticles exists, more pores are expected to be observed. Based on these results, the IN718-0.5 Y_2O_3 demonstrates highly favorable powder assembly effects and good LPBF build quality. As a result, it will be the primary focus of the subsequent detailed investigations to study the role of Y_2O_3 .

The characteristic microstructure of IN718 fabricated without the addition of Y_2O_3 using the LPBF process has been previously

Table 1. Porosity of the as-built samples.

As-built samples	Porosity [%]
Inconel 718 (IN718)	0.07 ± 0.03
IN718-0.5 Y_2O_3	0.17 ± 0.02
IN718-1 Y_2O_3	0.49 ± 0.04

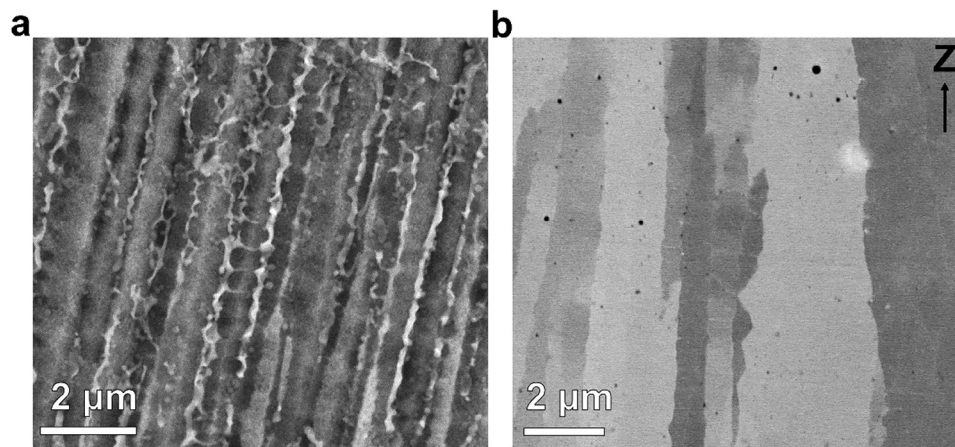


Figure 2. a) Secondary electron SEM imaging of columnar cells in as-printed IN718-0.5Y₂O₃ where the cell boundaries are in white indicating the presence of Laves phase; b) Backscattered electron SEM imaging of as-solutionized IN718-0.5Y₂O₃ sample where the columnar cell structures are retained while the Laves phase is dissolved.

reported.^[39–41] In our examination of the as-built IN718-0.5Y₂O₃, we observed a similar microstructure, as shown in **Figure 2a**, which displays the significant presence of Laves phase in the inter-dendritic regions. In this situation, the majority of the Y₂O₃ particles are obscured by Laves phase, making the analysis of Y₂O₃ challenging. To overcome this and to unambiguously identify the strengthening contribution of the sole yttria dispersoids, we employed a solution heat treatment on IN718-0.5Y₂O₃. An 1180 °C/1 h heat treatment results in the dissolution of almost all of the Laves phase, as confirmed by the scanning electron microscopy (SEM) image in **Figure 2b**. Meanwhile, numerous Y₂O₃ particles, indicated as black spots in the SEM-BSE image, become visible and easy to detect.

After the established one-step solution heat treatment scheme for IN718-0.5Y₂O₃, we proceeded to examine the tensile properties at ambient temperature; as displayed in **Figure 3**. The yield

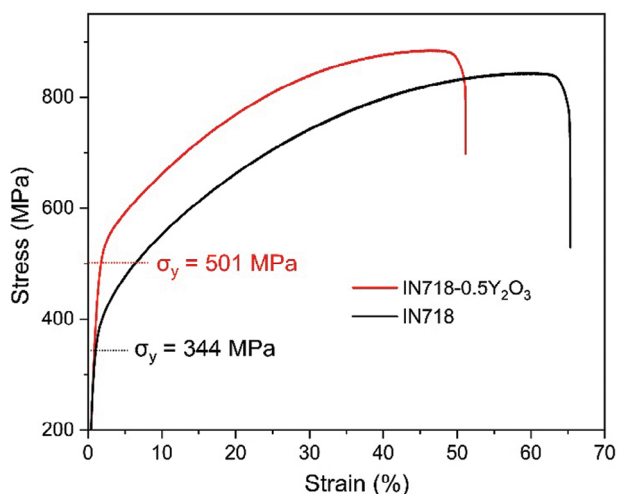


Figure 3. Room temperature tensile properties at a strain rate of $7 \times 10^{-4} \text{ s}^{-1}$ of LPBF-fabricated IN 718 and IN718-0.5Y₂O₃ after an 1180 °C/1 h solution heat treatment. Each curve is representative of three tensile tests with negligible scatter amongst them.

stress of pure IN718 in the solid solution state (without yttria particles) was measured to be 344 MPa, with an elongation (to failure) of over 60%. Upon incorporating 0.5 wt.% Y₂O₃, the yield stress increased to 501 MPa, although a (minor) drop in elongation to approximately 47% was noted. The strength increase represents a substantial gain of 157 MPa, which translates to a 46% improvement compared to the pure IN718 alloy. In addition, the ultimate tensile strengths (UTS) of as-solutionized pure IN718 and IN718-0.5Y₂O₃ are measured as 844 MPa and 874 MPa, respectively.

In order to understand the underlying reasons behind the substantial strength increase resulting from the addition of (only) 0.5 wt.% Y₂O₃, we further investigated the grain structure in both solution-treated IN718 and IN718-0.5Y₂O₃ specimens by inverse pole figure (IPF) mapping and geometrically necessary dislocation (GND) mapping. **Figure 4a,b** reveals the characteristic and uniformly recrystallized microstructure of the solution-treated IN718 sample. This further supports that 1180 °C/1 h solution heat treatment can result in full recrystallization in IN718, consistent with previous work.^[42] Conversely, the IPF and GND mapping images of the IN718-0.5Y₂O₃ counterparts (**Figure 4c,d**) display notable differences. Specifically, some high dislocation storage areas (green color in **Figure 4d**) appear and, thus, the microstructure appears to be heterogeneous. This underpins that the presence of Y₂O₃ nanoparticles has influenced the recrystallization and/or dislocation recovery processes in the IN718 alloy. To establish a correlation between low-angle grain boundaries (LAGBs), defined by boundary rotation angles of less than 15°, and GNDs, **Figure 4f** presents an enlarged region characterized by high densities of additional dislocation storage. For comparison purposes, the boundary rotation angle map (**Figure 4e**) is given at the same scale. The correspondence between LAGBs and regions exhibiting elevated GND densities becomes apparent, underscoring their interrelationship. However, the precise role played by the nanoscale dispersion of Y₂O₃ in retaining these regions of high GND density within the IN718-0.5Y₂O₃ samples remains unclear. Further exploration of this topic will be addressed next with the aid of TEM.

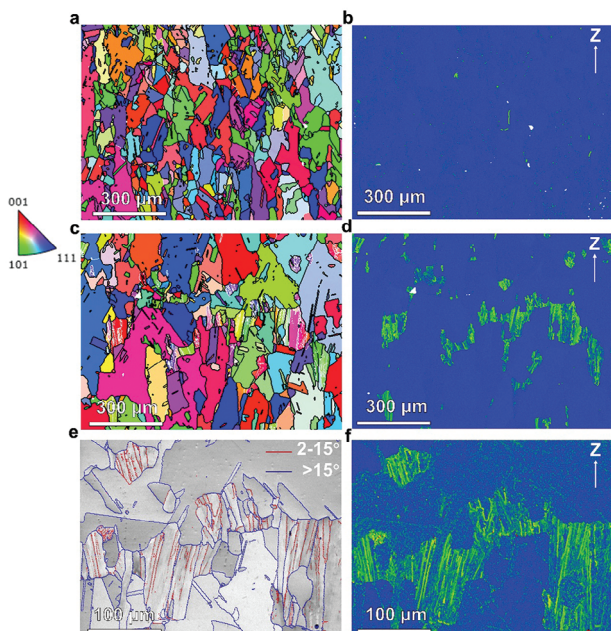


Figure 4. a) IPF and b) corresponding GND maps showing the grain microstructure of LPBF IN718 after 1180 °C/1 h solution heat treatment; c) IPF and d) corresponding GND maps showing the grain microstructure of LPBF IN718-0.5Y₂O₃ after 1180 °C/1 h solution heat treatment; e) a detailed grain boundary map of a high GND density region in the as-solutionized IN718-0.5Y₂O₃ with boundary rotation angle lines indexed; f) the corresponding GND map of as-solutionized IN718-0.5Y₂O₃.

Due to the existence of two different grain areas with different amounts of dislocation storage in the solution-treated IN718-0.5Y₂O₃ sample, the focused ion beam (FIB) technique was employed to lift out samples in these two areas to gain direct insights into the distribution of Y₂O₃ nanoparticles in these two areas. By employing bright-field (BF) scanning transmission electron microscopy (STEM) and corresponding energy-dispersive X-ray spectroscopy (EDS) mapping, the Y₂O₃ distributions within these regions are visualized (Figure 5b,e). Convergent-beam electron diffraction (CBED) was used to measure the thickness of the observed areas. The results for the thicknesses of the regions with low and high dislocation storage densities were measured to be 138 nm and 95 nm, respectively. It is important to note that the EDS signal collection parameters, such as dwell time and frames, were kept identical for each map, ensuring comparability of the results presented in Figure 5b,e. As a consequence, the volume fractions of Y₂O₃ were determined to be 0.26% and 1.37% in the regions with low and high extra dislocation storage densities, respectively. This clearly demonstrates a direct interrelation between Y₂O₃ dispersion volume fraction and dislocation storage density.

The presence of a higher concentration of Y₂O₃ nanoparticles within regions characterized by elevated dislocation storage densities suggests that the Y₂O₃ particles play a significant role in retarding dislocation motion, and so also recovery and recrystallization processes. This observation is further supported by the two-beam condition bright-field transmission electron microscopy (BF-TEM) images presented in Figure 6, which depict the interactions between individual Y₂O₃ nanoparticles

and dislocations.^[43,44] The BF-TEM images reveal that the Y₂O₃ nanoparticles not only interact with individual dislocations but also impede the movement of LAGBs. These interactions provide evidence that the Y₂O₃ nanoparticles are effective pinning sites, hindering the glide and propagation of both individual dislocations and LAGBs. The Burgers vector (*b*) of these dislocations is confirmed to be ½ <110> based on the results of diffraction contrast experiments, i.e., making use of the criterion of dislocation image invisibility when *g*·*b* = 0.

The increment of yield strength in the solution-treated IN718-0.5Y₂O₃ ($\Delta\sigma_y$) can in essence be expressed as the sum of dispersion strengthening ($\sigma_{\text{dispersion}}$) and dislocation strengthening effect ($\Delta\sigma_{\text{dislocation}}$)^[45] based on the presence of nano-sized oxide particles and retained dislocations. However, the grain size of IN718-0.5Y₂O₃ is larger than IN718 so the Hall-Petch strengthening effect ($\Delta\sigma_{\text{Hall-Petch}}$) of IN718-0.5Y₂O₃ will be negative to the yield strength. The whole $\Delta\sigma_y$ is written as following:

$$\Delta\sigma_y = \sigma_{\text{dispersion}} + \Delta\sigma_{\text{dislocation}} - \Delta\sigma_{\text{Hall-Petch}} \quad (1)$$

It is generally accepted that the dispersion strengthening effect at room temperature resulting from hard and non-shearable particles can be directly calculated by the Orowan bypass equation:^[22,46]

$$\sigma_{\text{dispersion}} = \sigma_{\text{Orowan}} = 0.13M \frac{Gb}{\sqrt{1-\nu}} \frac{\ln\left(\frac{2.45 \cdot R}{b}\right)}{\lambda} \quad (2)$$

where *M* is Taylor factor, *b* is magnitude of Burgers vector, *G* is shear modulus, ν is Poisson ratio, *R* is the mean radius of oxide particles. The effective interparticle spacing, λ , is influenced by the volume fraction of the particles in the observation region (ϕ) and calculated according to:^[22]

$$\lambda = \left[\left(\frac{3\pi}{4\phi} \right)^{\frac{1}{2}} - 1.64 \right] R \quad (3)$$

Inserting calculation of λ into Equation 2 after the measurement of ϕ , the dispersion strengthening effects can be predicted.

It is also evident from the microstructural investigations that $\sigma_{\text{dispersion}}$ of the solution treated IN718-0.5Y₂O₃ should be modified as the weighted average dispersion strengthening effect, $\Delta\sigma_{\text{dispersion}}$, according to the fraction of low and high dislocation storage regions (refer to Figure 4d):

$$\sigma_{\text{dispersion}} = \Delta\sigma_{\text{dispersion}} = k\sigma_{\text{high}} + (1-k)\sigma_{\text{low}} \quad (4)$$

where *k* is the fraction of the high dislocation density region, σ_{high} and σ_{low} is the dispersion strengthening effects of the high and low dislocation density region, respectively. The values of *R* and ϕ have been measured based on Figure 5 above and, thus, the dispersion strengthening effects could be calculated for two different dislocation density regions. According to Equation 4, the calculated value of $\sigma_{\text{dispersion}} \approx 114$ MPa. Corresponding parameters are summarized in Table 2

$\Delta\sigma_{\text{dislocation}}$ is the differences in the dislocation strengthening effects between fully annealed IN718 and the as-solutionized

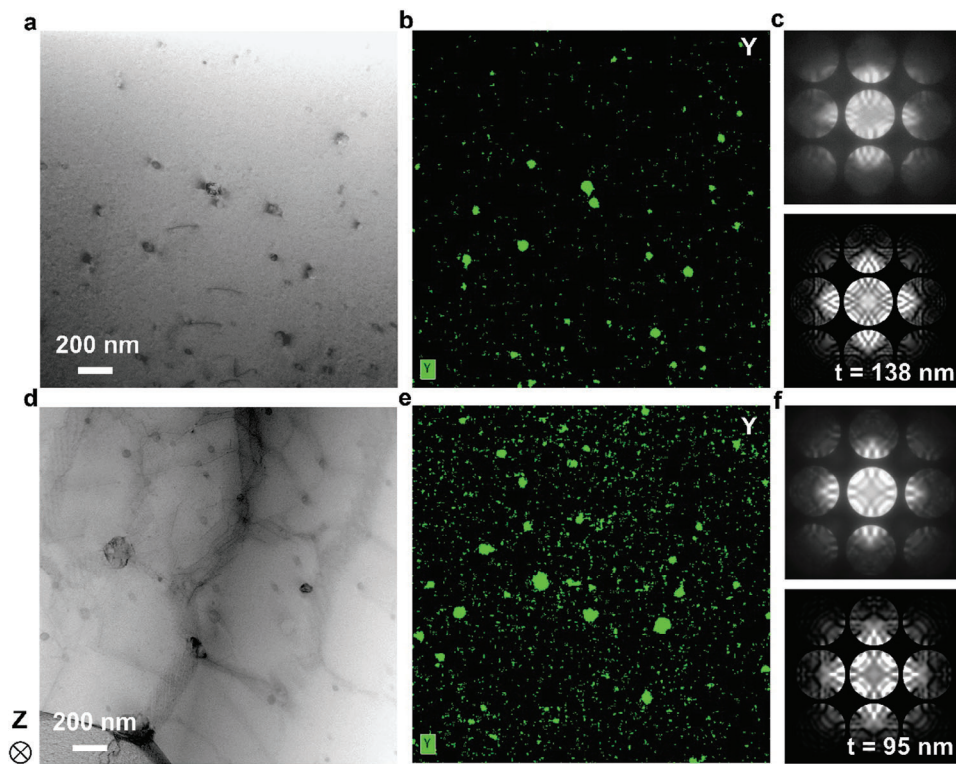


Figure 5. a) and d) BF-STEM images showing the distribution of Y_2O_3 in the low and high dislocation storage density regions respectively of the as-solutionized IN718-0.5 Y_2O_3 FIB samples; b) and e) Corresponding STEM-EDS maps showing the Y distribution to indicate the Y_2O_3 particles; c) and f) Experimental CBED patterns (top) and specimen thickness-based simulation CBED patterns (bottom) in the low and high dislocation storage density regions respectively (the zone axes are both $[100]$) used for foil thickness measurements).

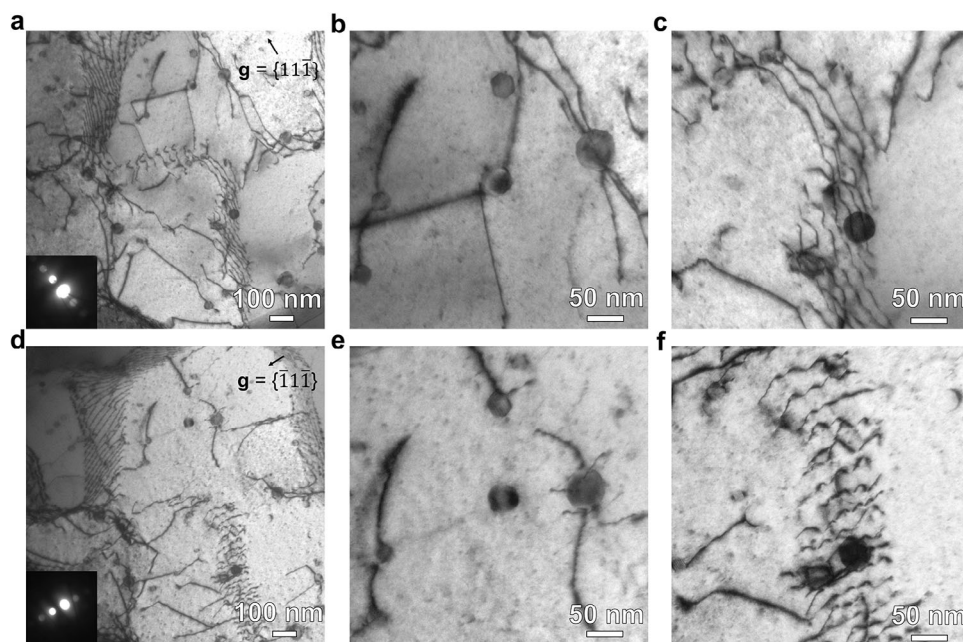


Figure 6. Two-beam diffraction condition BF-TEM images of dislocations, which are pinned by nano Y_2O_3 particles in a high dislocation storage density region of the as-solution IN718-0.5 Y_2O_3 sample. Dislocation-particle interaction is apparent, both for individual dislocations as well as for (retained) LAGB: a, d) Overview of these regions where nano Y_2O_3 particles interact with individual dislocations in the matrix and the retained LAGB, and the g vectors are shown at the top right corners, inserts are the corresponding diffraction patterns to show the g vectors in zone axis $[110]$; b, e) Individual dislocations of which the Burgers vectors are determined as $b = \frac{1}{2} \langle 110 \rangle$ pinned by nano Y_2O_3 particles; c, f) Nano Y_2O_3 particles interacting with LAGBs.

Table 2. Parameters for calculation of dispersion strengthening effects.

Parameters	M	B [nm]	G [GPa]	ν	R [nm]	Φ [%]	k
	3.07	0.25	79	0.3	20	0.26 ^{a)} /1.37 ^{b)}	0.25

^{a)} (Y_2O_3 volume fraction from low dislocation density region); ^{b)} (Y_2O_3 volume fraction from high dislocation density region).

IN718-0.5 Y_2O_3 , which is related to the mean density of dislocations (ρ) and can be calculated by^[47,48]

$$\Delta\sigma_{\text{dislocation}} = M\beta Gb(\rho)^{1/2} \quad (5)$$

where M , G , and b have the same meaning as above and β is a coefficient with a value of 0.2 for face-centered cubic (FCC) crystal structure. Here, for simplification, the value of ρ used in Equation 4 refers to the GND density rather than to the total dislocation density, which also includes statistically stored dislocations (SSD). Moreover, as ρ in well annealed IN718 is negligible compared with as-solutionized IN718-0.5 Y_2O_3 due to the dislocations that are pinned by Y_2O_3 , see Figure 4b,d, ρ can merely be measured as $0.19 \times 10^{14}/m^2$ by the GND maps of IN718-0.5 Y_2O_3 . The dislocation strengthening effect of IN718-0.5 Y_2O_3 can be calculated as 51 MPa.

The grain boundary strengthening is described mathematically by the Hall-Petch equation^[49,50] and, in this case, the $\Delta\sigma_{\text{Hall-Petch}}$ is the differences between IN718 and IN718-0.5 Y_2O_3 :

$$\Delta\sigma_{\text{Hall-Petch}} = k_y[(d_{\text{IN718}})^{-1/2} - (d_{\text{IN718-0.5Y}})^{-1/2}] \quad (6)$$

where k_y is the strengthening coefficient for Ni (428.17 MPa $\mu\text{m}^{-1/2}$) and d is the grain size. According to Figure 4, the averaged grain size of IN718 (d_{IN718}) and IN718-0.5 Y_2O_3 ($d_{\text{IN718-0.5Y}}$) is 119 μm and 235 μm respectively. Then, the value of $\Delta\sigma_{\text{Hall-Petch}}$ based on Equation 6 is calculated as 9 MPa.

In summary, the predicted $\Delta\sigma_y$ is ≈ 156 MPa according to Equation 1, which is close to the increase of yield stress, 157 MPa, measured by tensile tests (as shown in Figure 3).

3. Conclusion

In summary, this study represents a pioneering effort to utilize the combined ESA and LPBF approach to produce ODS IN718 superalloys. Significant strengthening effects have been achieved, as evidenced by a remarkable 46% improvement in room-temperature yield strength, with the addition of 0.5 wt.% of Y_2O_3 nanoparticles. Further microstructural observations reveal that this strengthening effect can be attributed to the Y_2O_3 dispersion strengthening and dislocation strengthening of a heterogeneous microstructure. The results pave the way for the development of new ODS alloy designs tailored for additive manufacturing, holding immense potential to advance the field of AM in the production of high-performance ODS materials. In addition, the results open up intriguing possibilities for strategically manipulating the heterogeneous microstructures to optimize the balance between strength and ductility in ODS Ni-based superalloys.

4. Experiments Section

Electrostatic Self-Assembly Powder Preparation: Gas-atomized IN718 virgin powders were supplied by Carpenter Company and decorated by 2 different nominal contents of nano-yttria particle mass fractions (Y_2O_3 , 0.5 wt.% and 1 wt.%, the samples named IN718-0.5 Y_2O_3 and IN718-1.0 Y_2O_3 respectively.), which were provided by Aladdin Biochemical Technology Co., Ltd., through the ESA method. The pH values of both the polyelectrolytes of IN718 and Y_2O_3 were carefully controlled between 8 to guarantee the negative charge of IN718 and Y_2O_3 particles. With the ESA method (as illustrated in Figure 7.), IN718 raw powder materials were dispersed and stirred in a (3-aminopropyl) triethoxysilane (APTES, $C_9H_{23}NO_3Si$, chemical pure) modified solution for the purpose of introducing positive charges, Figure 7a. Then, in order to create negative charges on the nano Y_2O_3 particles, a sodium dodecyl sulfate (SDS, $NaC_{12}H_{25}SO_4$, analytical reagent) modified solution was used, Figure 7b. Two solutions with these opposite charges were then mixed and stirred for 2 h, Figure 7c, and the suspension (mixture of IN718 and nano Y_2O_3) was filtered under a vacuum environment of 1 bar. The wet powder mixture was transferred into a freeze dryer at -40°C for 12 h. Composites consisting of large IN718 particles (grey in Figure 7d) and nano yttria particles electrostatically attached to them (green) were created by this approach.

LPBF Processing and Heat Treatments: The LPBF process was performed using a GINM-D150 self-developed machine equipped with a 500 W Ytterbium fibre laser with a beam diameter of $\approx 40 \mu\text{m}$. The printing process was operated with a base plate temperature of 80°C available for the LPBF machine to alleviate thermal stresses and to prevent subsequent cracking. Laser parameters with low energy density were specifically used to reduce crack susceptibility as discussed elsewhere for similar superalloys.^[25,26] The laser power and scanning speed were maintained at 170 W and 1200 mm^{-1}s respectively, and the layer thickness was set to 20 μm . A custom scanning strategy incorporating a 67° rotation between each layer was applied in this work. The 3D directions of the as-printed specimens were designated as building direction (Z), horizontal direction (X) and normal direction (Y), where Z was parallel to the building direction of stacking layers, X was parallel to the roller moving direction, and Y was perpendicular to the roller moving direction. With the optimization of alloy composition, processing parameters and powder control in LPBF, cubic samples ($10 \times 10 \times 5 \text{ mm}^3$) were created for microstructural investigation while dog-bone shape samples (25 mm gauge length and 3 mm width for deformation segment, 3.5 mm in thickness) were fabricated for the room temperature tensile property measurements. After LPBF, a group of cubic samples and dog-bone shape tensile samples were heat treated under the temperature of 1180 $^\circ\text{C}$ for 1 h (protected by argon atmosphere) followed by air cooling to room temperature.

Measurements and Characterizations: The chemical composition of as-printed IN718 samples with and without Y_2O_3 was measured by inductively coupled plasma optical emission spectroscopy (ICP-OES, Agilent 720ES). The melt defects and/or porosity measurements of all as-printed specimens were observed through Leica DMI 5000 M optical microscopy (OM) system. XZ cross-sections of three bulk samples of each as-printed IN718 with and without Y_2O_3 modification were ground and polished for porosity measurements. For a single measurement, five regions were selected based on the five-point sampling method and the area fractions of porosity were calculated by ImageJ software and averaged. The morphology of powders with different Y_2O_3 contents and the microstructure of all as-printed and as-solution specimens were evaluated by scanning electron microscopy (SEM, JEOL 7001-F and FEI Quanta 3D FIB) with integrated electron backscatter diffraction (EBSD) mode. For SEM observation, specimens were finely ground (from 360# to 3000# sandpaper) and polished to reveal all relevant microstructural details, i.e., the Laves phase and the distribution of nano Y_2O_3 particles. EBSD was used to quantitatively analyze the grain size, grain boundary misorientation, grain orientation and crystallographic texture. For EBSD analysis, specimens were mechanically polished and subsequently electropolished with an electrolyte containing 20 ml perchloric acid and 80 ml ethanol mixture. At even higher magnification, dislocations and their interaction with Y_2O_3 dispersion were investigated by transmission electron microscopy (TEM) using a FEI Tecnai T20

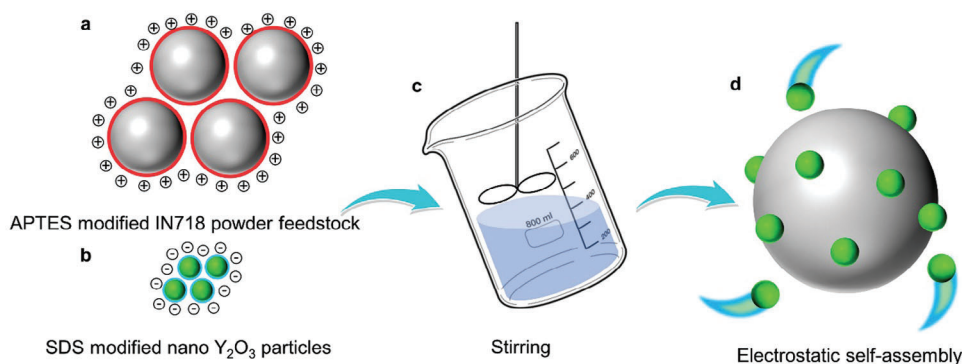


Figure 7. Schematic synthesis of IN718 powder modified by nano Y_2O_3 particles by electrostatic self-assembly (ESA) method. a) Positive charges are generated on the surface of IN718 powder feedstock; b) Negative charges are generated on the surface of yttria particles; c) Two powders are stirring and mixing in a solution; d) IN718 particle attracts yttria nanoparticles due to opposite charges.

operated at 200 kV. The scanning TEM (STEM) images and corresponding energy-dispersive X-ray spectroscopy (EDS) maps under STEM mode were obtained from the FEI Tecnai F20 field emission gun (FEG) at 200 kV to visualize the size and distribution of Y_2O_3 . The specimens for all the TEM analyses were first ion milled and lifted out subsequently utilizing a focused ion beam (FIB) SEM (Thermo Scientific Helios 5 UX DualBeam). Tensile tests were performed to investigate the mechanical properties of the as-solutionized specimens along the horizontal direction (the transverse specimen). The experiments were carried out at room temperature under quasi-static loading (strain rate of $7 \times 10^{-4} \text{ s}^{-1}$ in the gauge section) according to the ASTM E8-08 standard test method for tension testing of metallic materials, using a GOPOINT GJZX-A0004 universal tensile testing machine. For each condition, three tensile tests were conducted.

Acknowledgements

The authors gratefully acknowledge the scientific and technical assistance at the Monash Centre for Additive Manufacturing (MCAM) and Monash Centre for Electron Microscopy (MCEM) as a Node of Microscopy Australia. The authors are grateful for the financial support from the Australian Research Council (LP220100400). This research used equipment funded by Australian Research Council grants: FEI Tecnai G2 F20 S-TWIN FEGTEM (LE110100223) and Thermo Fisher Scientific Helios 5 UX FIB-SEM (LE200100132). S.B.D. and S.W. wish to thank the financial support from the Monash Graduate Scholarship.

Open access publishing facilitated by Monash University, as part of the Wiley - Monash University agreement via the Council of Australian University Librarians.

Conflict of Interest

The authors declare no conflict of interest.

Data Availability Statement

The data that support the findings of this study are available from the corresponding author upon reasonable request.

Keywords

electrostatic self-assembly, heterogeneous microstructure, laser powder bed fusion, oxide dispersion strengthened superalloy, yield strength

Received: September 30, 2023
Published online:

- [1] J. Wang, W. Yuan, R. S. Mishra, I. Charit, *J. Nucl. Mater.* **2013**, *442*, 1.
- [2] P. A. Molian, Y. M. Yang, P. C. Patnaik, *J. Mater. Sci.* **1992**, *27*, 2687.
- [3] G. B. Schaffer, M. H. Loretto, R. E. Smallman, J. W. Brooks, *Acta Mater.* **1989**, *37*, 2551.
- [4] S. K. Kang, R. C. Benn, *Metall. Mater. Trans. A* **1987**, 747.
- [5] M. B. Wilms, S.-K. Rittinghaus, M. Goßling, B. Gökce, *Prog. Mater. Sci.* **2023**, 133.
- [6] C. T. Sims, N. S. Stoloff, W. C. Hagel, *Superalloys II: High-Temperature Materials for Aerospace and Industrial Power*, **1987**.
- [7] J. S. Benjamin, *Metallurgical Transactions* **1970**, *1*, 2943.
- [8] C. Suryanarayana, E. Ivanov, V. V. Boldyrev, *Mater. Sci. Eng., A* **2001**, *304–306*, 151.
- [9] W. He, F. Liu, L. Tan, Z. Tian, Z. Qin, L. Huang, X. Xiao, G. Wang, P. Chen, B. Liu, *Materials* **2022**, 15.
- [10] W. He, F. Liu, L. Tan, L. Huang, Y. Nie, G. Wang, X. Zhan, Z. Qin, *Mater. Today Commun.* **2021**, 26.
- [11] L. Tan, G. Wang, Y. Guo, Q. Fang, Z. Liu, X. Xiao, W. He, Z. Qin, Y. Zhang, F. Liu, L. Huang, *Virtual Phys. Prototyp.* **2020**, *15*, 555.
- [12] S. Ma, A. Li, S. Zhou, Y. Yang, S. Wang, M. Liu, *J. Alloys Compd.* **2018**, *750*, 911.
- [13] S. Pasebani, A. K. Dutt, J. Burns, I. Charit, R. S. Mishra, *Mater. Sci. Eng., A* **2015**, *630*, 155.
- [14] X. Yan, S. Gao, C. Chang, J. Huang, K. Khanlari, D. Dong, W. Ma, N. Fenineche, H. Liao, M. Liu, *J. Mater. Process. Technol.* **2021**, 288.
- [15] C. Guo, Z. Yu, X. Hu, G. Li, F. Zhou, Z. Xu, S. Han, Y. Zhou, R. M. Ward, Q. Zhu, *Compos. B. Eng.* **2022**, 230.
- [16] J. H. Martin, B. D. Yahata, J. M. Hundley, J. A. Mayer, T. A. Schaedler, T. M. Pollock, *Nature* **2017**, *549*, 365.
- [17] T. M. Smith, C. A. Kantzos, N. A. Zarkevich, B. J. Harder, M. Heczko, P. R. Gradl, A. C. Thompson, M. J. Mills, T. P. Gabb, J. W. Lawson, *Nature* **2023**.
- [18] B. M. Arkhurst, J.-J. Park, C.-H. Lee, J. H. Kim, *Korean J. Met. Mater* **2017**, 55.
- [19] X. Duan, S. Gao, Q. Dong, Y. Zhou, M. Xi, X. Xian, B. Wang, *Surf. Coat. Technol.* **2016**, *291*, 230.
- [20] G. Yuling, W. Meiping, M. Xiaojin, C. Chen, *Adv. Mech. Eng.* **2021**, 13.
- [21] M. Li, L. Wang, H. Yang, S. Zhang, X. Lin, W. Huang, *Mater. Sci. Eng., A* **2022**, 854.
- [22] C. Kenel, A. De Luca, S. S. Joglekar, C. Leinenbach, D. C. Dunand, *Addit. Manuf.* **2021**, 47.
- [23] J. U. Rakhmonov, C. Kenel, A. De Luca, C. Leinenbach, D. C. Dunand, *Additive Manufacturing Letters* **2022**, 3.
- [24] G. Wang, L. Huang, L. Tan, Z. Qin, C. Chen, F. Liu, Y. Zhang, *Mater. Sci. Eng. A* **2022**, 859.

- [25] Q. Song, Y. Zhang, Y. Wei, X. Zhou, Y. Shen, Y. Zhou, X. Feng, *Opt. Laser Technol.* **2021**, 144.
- [26] D. N. Luu, W. Zhou, S. M. L. Nai, *Mater. Sci. Eng., A* **2022**, 845.
- [27] D. N. Luu, W. Zhou, S. M. L. Nai, *Mater Sci Add Manuf* **2022**, <https://doi.org/10.18063/msam.v1i4.25>.
- [28] M. Yesim Yalcin, D. Bora, E. Aydogan, *J. Alloys Compd.* **2022**, 914.
- [29] C. Doñate-Buendia, P. Kürsteiner, F. Stern, M. B. Wilms, R. Streubel, I. M. Kusoglu, J. Tenkamp, E. Bruder, N. Pirch, S. Barcikowski, K. Durst, J. H. Schleifenbaum, F. Walther, B. Gault, B. Gökce, *Acta Mater.* **2021**, 206.
- [30] J. Yi, C. Chang, X. Yan, Y. Xie, Y. Liu, M. Liu, K. Zhou, *Mater. Charact.* **2022**, 191.
- [31] W. Zhou, K. Kikuchi, N. Nomura, K. Yoshimi, A. Kawasaki, *J. Alloys Compd.* **2020**, 819.
- [32] W. Zhou, K. Kamata, M. Dong, N. Nomura, *Powder Technol.* **2021**, 382, 274.
- [33] X. Cheng, Y. Zhao, Z. Qian, J. Wu, J. Dong, Z. Ma, Y. Liu, *Mater. Sci. Eng. A* **2021**, 824.
- [34] Y. Estrin, S. Arndt, M. Heilmaier, Y. Bréchet, *Acta Mater.* **1999**, 47, 595.
- [35] P. Susila, D. Sturm, M. Heilmaier, B. S. Murty, V. Subramanya Sarma, *Mater. Sci. Eng., A* **2011**, 528, 4579.
- [36] X.-H. Chen, H. Yan, *Mater. Des.* **2016**, 94, 148.
- [37] Y. Wang, J. Shi, *Appl. Phys. A* **2019**, 125.
- [38] M. Liu, L. N. S. Chiu, C. Vundru, Y. Liu, A. Huang, C. Davies, X. Wu, W. Yan, *Addit. Manuf.* **2021**, 44.
- [39] V. V. Rielli, A. Piglione, M.-S. Pham, S. Primig, *Addit. Manuf.* **2022**, 50.
- [40] W. M. Tucho, P. Cuvillier, A. Sjolyst-Kverneland, V. Hansen, *Mater. Sci. Eng., A* **2017**, 689, 220.
- [41] M. He, H. Cao, Q. Liu, J. Yi, Y. Ni, S. Wang, *Addit. Manuf.* **2022**, 55.
- [42] S. Wu, H. Z. Peng, X. Gao, P. D. Hodgson, H. Y. Song, Y. M. Zhu, Y. Tian, A. J. Huang, *Mater. Sci. Eng. A* **2022**, 857.
- [43] M. C. Brandes, L. Kovarik, M. K. Miller, G. S. Daehn, M. J. Mills, *Acta Mater.* **2012**, 60, 1827.
- [44] J. H. Schröder, E. Arzt, *Scr. Mater.* **1985**, 19, 1129.
- [45] P. M. Hazzledine, *Scr. Mater.* **1991**, 26, 57.
- [46] B. Reppich, *Acta Mater.* **1998**, 46, 61.
- [47] M. Ni, C. Chen, R. Xu, S. R. E. Hosseini, R. Li, X. Zhang, K. Zhou, *J. Alloys Compd.* **2022**, 918.
- [48] G. Taylor, *Proc. R. Soc* **1934**, 145, 362.
- [49] E. O. Hall, *Proc. Phys. Soc. B* **1951**, 64, 747.
- [50] N. J. Petch, *J. Iron Steel Institute* **1953**, 174, 25.